Supporting Information for

Hydrogen Evolution on Halogenated MXenes via Surface Termination Engineering: A Data-Informed Computational and Experimental Strategy

Ankita Kumari[1], Shivangi Singh[1], Ram Munde[2], Aejaz Ul Bashir[1], Pravin P. Ingole[1], Dibyajyoti Ghosh[1,2]**

1Department of Chemistry, Indian Institute of Technology, Delhi, Hauz Khas, New Delhi-110016, India

2 Department of Materials Science and Engineering (DMSE), Indian Institute of Technology, Delhi, Hauz Khas, New Delhi-110016, India

Section S1: Static Geometric Details

We perform first-principle calculations to understand the atomistic structure of halogen-terminated Ti_3C_2 MXenes at a three-fold hollow site formed by Ti atoms (H_{Ti}).[1,2] The structural details of pristine Ti_3C_2 and $Ti_3C_2T_2$ (T = F, Cl, Br, I) are included in Table S1. Table S1 shows the bond lengths between Ti-C and Ti-X. Additionally, the Ti-C bond lengths exhibit a slight increase with higher atomic numbers of the halogens, indicating a minimal effect of terminal groups on Ti-C bond strength. The optimized structures of pristine Ti_3C_2 and halogen-terminated ($Ti_3C_2T_2$) MXenes are shown in Figure S1a-d and Figure 1a.

Table S1:

Formula	Crystal Structure	d_{Ti1-C} (Å)	d_{Ti2-C}(Å)	d_{Ti2-T}(Å)
Ti_3C_2	Pristine	2.034	2.20	--
$Ti_3C_2F_2$	FCC	2.07	2.19	2.17
$Ti_3C_2Cl_2$	FCC	2.11	2.23	2.50
$Ti_3C_2Br_2$	FCC	2.13	2.26	2.63
$Ti_3C_2I_2$	FCC	2.15	2.29	2.81

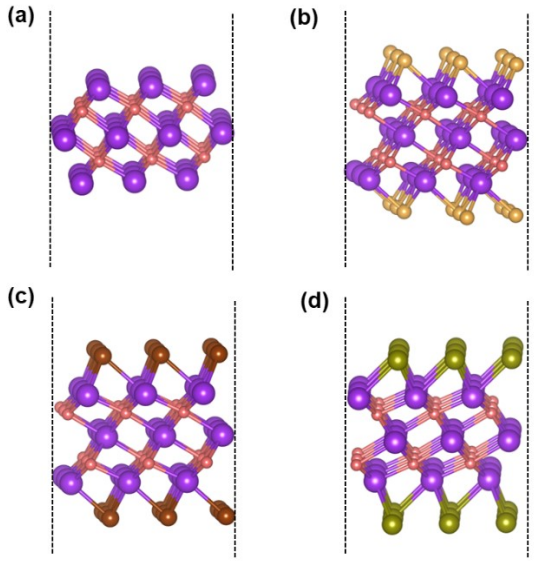

Figure S1: (a) *Optimized geometry of pristine Ti_3C_2 MXene.* ***(b-d)*** *Optimized geometries of $Ti_3C_2T_2$ (T = Cl, Br, I) MXenes. Color keys: purple (Ti), pink (C), golden (Cl), brown (Br), and olive green (I).*

Section S2: Static Electronic Details

The computed electronic structure provides valuable insights into the electronic properties of halogen-terminated MXenes near the Fermi level.[3,4] The plotted partial density of states (pDOS) plot in Figure S2a-d shows the metallic nature of halogen-terminated MXenes. The Ti 3d states prominently influence the Fermi level. We note that the pDOS plot for $Ti_3C_2T_2$ in Figure S2a-d reveals a notable increase in halogen states near the Fermi level with a change in T from F to Cl to Br to I, following the electronegativity order.

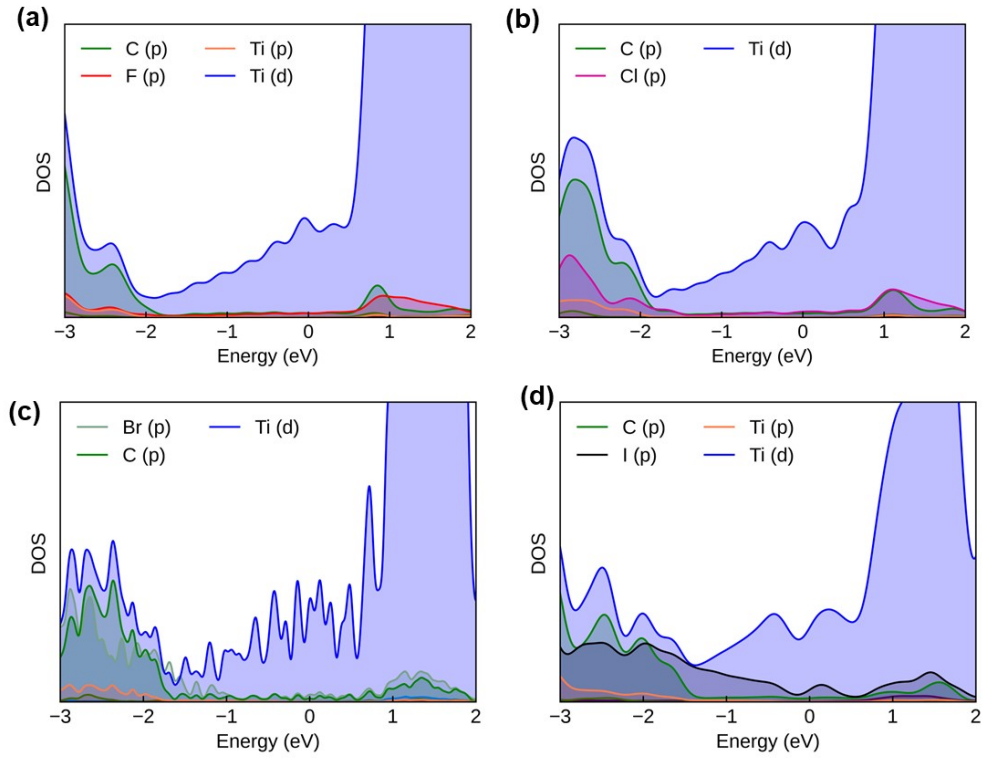

Figure S2: (a-d) *The partial density of states plot for $Ti_3C_2T_2$ MXenes (T = F, Cl, Br, and I).*

Section S3: Bonding Characteristics and Charge Distribution

To further study the charge distribution and electronic properties of halogen-terminated MXenes, we perform Bader charge and Electron Localization Function (ELF) analyses.[5,6] A quantitative estimation of charge transfer using the Bader charge analysis is presented in Figure S3e. Following the electronegativity difference (F > Cl > Br > I > C > Ti), the charge is transferred to the C and X atoms from the Ti. The trend in electron transfer from Ti to the

halogen atoms follows the order: F ($0.76e^-$) > Cl ($0.63e^-$) > Br ($0.56e^-$) > I ($0.46e^-$), where the values in brackets present the amount of electron transferred. This trend aligns with the relative electronegativities of the halogens, where higher electronegativity results in greater electron transfer from Ti.

The ELF reflects the bonding characteristics of the $Ti_3C_2T_x$ system in Figure S3a-d, where the maximum ELF = 1 corresponds to the perfect electron localization with respect to the uniform electron gas. On the other hand, ELF = 0.5 corresponds to electron-gas-like pair probability, and ELF = 0 indicates completely delocalized electrons. In systems with predominantly ionic character, ELF shows high localization around anions and low values in the regions between nuclei, indicating minimal electron sharing.[7] As shown in Figure S3a-d, electrons are mainly distributed around the C and X atoms, while fewer electrons are located around the metal (Ti). Such electron distribution is also evidenced by different colored regions in the ELF map. Based on the ELF map in Figure S3, the red-colored region around the C or X atoms indicated a marked electron transfer from metal to these atoms. For $Ti_3C_2F_2$, the ELF values reveal a low electron density between Ti and C atoms, accompanied by highly spherical localization around the F atoms. This pattern indicates a predominantly ionic bonding character, driven by the significant electronegativity difference between Ti and F atoms. As the halogen termination changes from Cl to Br to I, the ELF plots show progressively distorted electron localization patterns. These distortions are characterized by less symmetric and more spread-out lobes, signifying a gradual shift from purely ionic to mixed ionic-covalent bonding. The observed trend in ELF distributions emphasizes the role of halogen electronegativity in dictating bond polarity and electron localization.

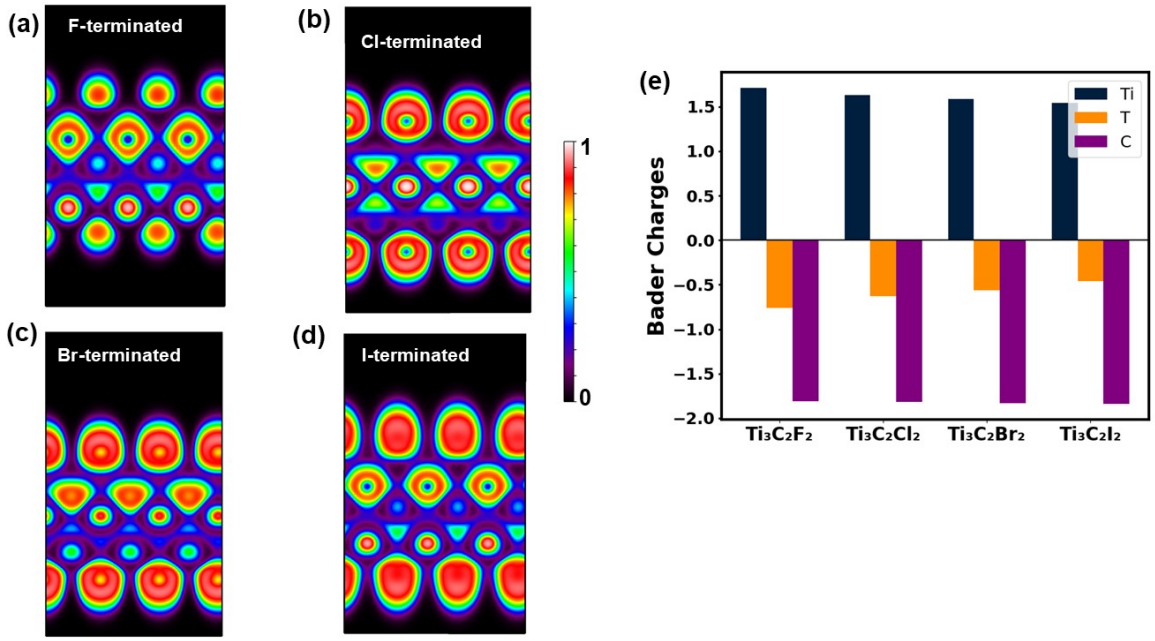

Figure S3: (a-d) *Electron localization function (ELF) plot for $Ti_3C_2T_2$ (T = F, Cl, Br, I) MXenes. The color scale is on the right.* ***(e)*** *The net bader charges on Ti, T, and C atoms, where the electron transfer from Ti to T follows the order: F>Cl>Br>I.*

Section S4: Electrocatalytic Hydrogen Evolution Reaction

The half-reaction HER can be expressed by the following two steps as per Volmer-Heyrovsky mechanism

$$* + H^+ + e^- = *H \quad (1)$$

$$*H + H^+ + e^- = *H_2 \quad (2)$$

During catalysis, intermediate species take part, necessitating their adsorption onto the catalyst's active sites for reliable configuration.[8,9] Optimized structures are used to calculate the Gibbs free energy to further analyze the halogen-terminated MXenes catalytic activity. The optimized structure of H_{ads} on fully -F and -Cl terminated MXenes is shown in Figure S4a-b. The adsorption energies for hydrogen adsorption have been calculated using the formula:

$$\Delta E_{H^*} = E_{Ti3C2+H} - E_{Ti3C2} - 1/2\, E_{H2}$$

Where $E_{Ti3C2+H}$ is the energy of the system with adsorbed hydrogen, E_{Ti3C2} is the energy of the pristine system, and E_{H2} is the energy of gaseous hydrogen. To calculate the HER activity of catalysts, the hydrogen adsorption-free energy (ΔG_H) is typically measured.[10]

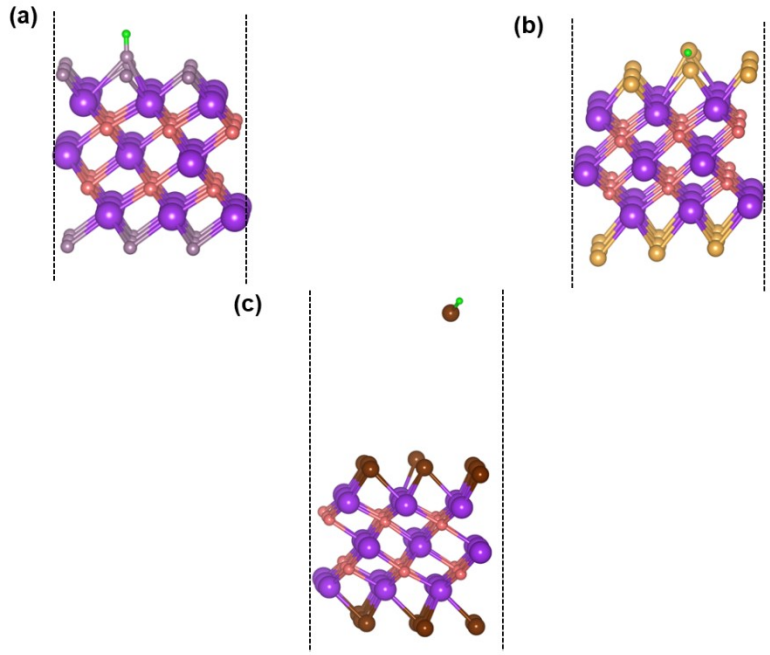

Figure S4: *Top view of chemical structures of reaction intermediates for H adsorbed on the* ***(a)*** *$Ti_3C_2F_2$ and* ***(b)*** *$Ti_3C_2Cl_2$ MXenes,* ***(c)*** *AIMD structure obtained after heating of $Ti_3C_2Br_2$ MXene.*

Section S5: Experimental Section: Materials and Chemicals, Synthesis (F-and Cl-terminated $Ti_3C_2T_2$ MXenes), Material Characterization, and Electrochemical Investigation

Materials and Chemicals: MAX phase powder, Ti_3AlC_2 (312, > 90 wt. % purity; < 45 µm particle size), is procured from Sigma Aldrich (Merck). Hydrogen fluoride (HF, 98.5%), Hydrogen Sulfate (H_2SO_4 98%), and HCl (35%, specific gravity ~1.18 g/mL) are purchased from Merck Life Science Pvt. Ltd. (Sigma Aldrich). Zinc Chloride ($ZnCl_2$, 98%), Zinc Sulfide (ZnS powder, 10 µm, 99.99%), urea (NH_2CONH_2, 98%), potassium chloride (KCl, 98%), Ethylene diamine (EDA), Nafion (5 wt.%), and glassy carbon (GC) plates are also purchased from Sigma Aldrich.

Synthesis: We experimentally validate our computational findings by synthesizing F- and chlorine-terminated Ti_3C_2 MXenes using established chemical etching methods. The optimized synthesis of Cl-terminated MXene is achieved using the molten salt etching method with a well-known top-down approach.[11] Typically, the Ti_3AlC_2 MAX phase and etchant $ZnCl_2$ ratio is maintained at 1:6, and the reaction is performed in a tube furnace under a constant N_2 flow at 640 ºC for 4 hours.[12] The reaction mixture is then washed with 4M HCl to remove excess

Zn, yielding a black powder of Cl-terminated MXenes. For the synthesis of F-terminated MXene, 2 g of Ti_3AlC_2 is directly etched with 48% HF at 60 °C for 48 hours, followed by washing (centrifugation) with water and an aqueous solution of KCl to obtain a colloidal solution of F-terminated MXenes. The colloidal solution is then dried in a Petri dish at 60 °C for 4 hours, followed by further drying in a vacuum oven at 60 °C for subsequent analysis. The overall synthesis protocol is depicted in Scheme 1.

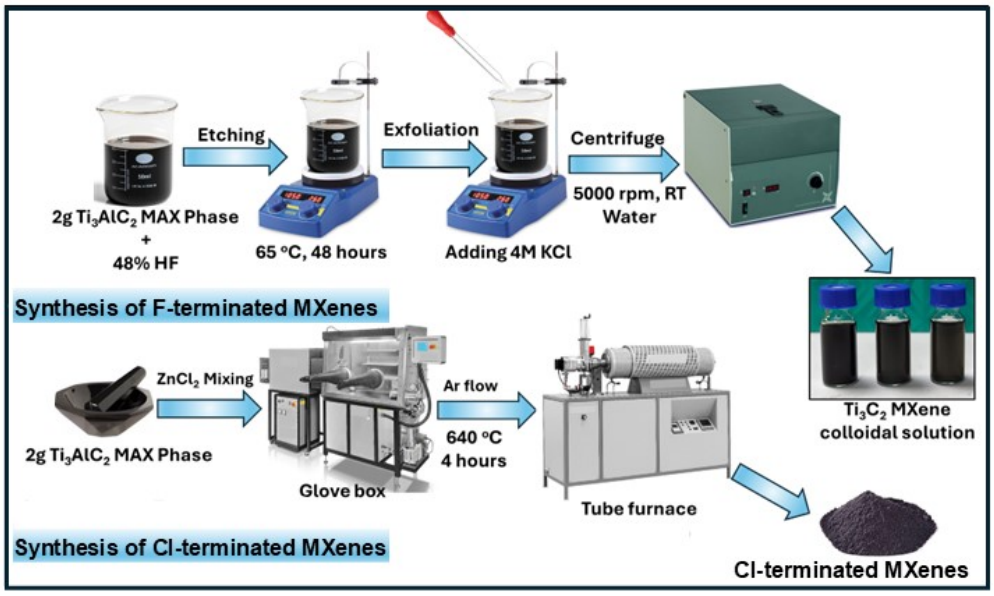

Scheme 1: *A detailed protocol followed for the synthesis of -F and Cl-terminated MXenes using chemical HF etching, molten $ZnCl_2$ salt etching, and hydrothermal treatment, respectively.*

Material Characterization: The crystal structure and phase purity of the synthesized MXenes were analyzed using powder X-ray diffraction (pXRD) on a Bruker D8 Advance X-ray diffractometer (US) equipped with Ni-filtered Cu K_α radiation (λ = 1.54 Å). Surface functionalities are characterized via Fourier transform infrared (FTIR) spectroscopy using a Nicolet Protégé 460 spectrometer within the 500-4000 cm^{-1} range. The morphology of the synthesized MXenes is examined through transmission electron microscopy (TEM) using a ThermoFisher Scientific instrument operating at 120 kV. X-ray photoelectron spectroscopy (XPS) performed on a PHI 5000 Versa Probe III instrument is employed to determine the chemical state of elements. Finally, hydrogen (H_2) quantification is conducted using gas chromatography (Thermo Scientific Trace 1110) with a thermal conductivity detector (TCD).

Electrochemical Investigations: All ex-situ electrochemical measurements are conducted using a Metrohm Autolab 302 electrochemical workstation in a custom-designed two-chamber,

three-electrode cell setup. The cathodic half-cell comprised a catalyst-ink-coated working electrode, prepared by drop-casting a mixture of 2 mg of catalyst in 100 µL isopropyl alcohol and 20 µL of 5% Nafion binder onto a 1 x 2 cm^2 glassy carbon (GC) plate electrode. An Ag/AgCl/Cl^- (sat. KCl) electrode (E^o = 0.197 V vs. RHE) served as the reference electrode, while a Pt-mesh counter electrode is immersed in 0.05 M H_2SO_4 in the anodic chamber. All the potentials are reported vs. RHE using the equation; $E_{RHE} = E_{Ag/AgCl,Cl^-(sat.KCl)} + 0.197 + 0.059\,pH$.

Section S6: XRD, FTIR, and Raman Spectra

Characterization: The optimized synthesis, crystal structure, and phase purity of the Cl-terminated MXenes are investigated using XRD patterns recorded within 2θ range of 5-80° as shown in Figure S5a. The pure phase of Cl-terminated MXene is obtained at the reaction conditions of 640° C temperature and four hours of reaction time (Scheme 1). Upon etching with Lewis acid $ZnCl_2$, the most intense non-basal peak at 2θ of 39°, corresponding to the (104) plane of Ti_3AlC_2, disappeared, and the peak at 9.53° for the basal plane (002) shifted to 7.58°, confirming the MXene formation.[12,13] The shifting of the (002) plane suggests an increase in the $d_{(002)}$-spacing from 9.27 Å for Ti_3AlC_2 MAX phase to 11.65 Å for Cl-Ti_3C_2, which again suggests successful etching of Aluminium and exfoliation of MXene sheets (Figure S5a). However, for F-terminated and doped samples, there is a slightly more 2θ shift for the (002) plane compared to Cl-terminated due to the intercalation of water and other cations during synthesis. Moreover, for F-terminated, the (002) reflection is relatively broader due to its more amorphous nature.[14]

The FTIR spectra for MXenes, as shown in Figure 2b, are segregated into two main regions: the lower frequency region (400-1200 cm^{-1}) corresponds to the fingerprint region, and the higher frequency region (1200-4000 cm^{-1}) is attributed to the carbon backbone and confined water within the MXene layers.[15] The Ti-Cl wagging mode (648 cm^{-1}) and anti-symmetric C-Cl (809 cm^{-1}) indicates successful *Cl functionalization, while the appearance of Ti-F wagging mode (800 cm^{-1}) and anti-symmetric C-F stretching mode (1115 cm^{-1}) is due to the *F functionalization of Ti_3C_2 MXene.[16,17] Moreover, the broad bands obtained at 3500 cm^{-1} and 1600 cm^{-1} correspond to -OH stretching (E_u) and bending modes (A_{2u}). The Raman spectra of the Ti_3AlC_2 MAX phase depict eight phonon bands at 128.3,146.1, 266.1, 394.2, 593.1, 633.2, 1387.1 and 1562.1 cm^{-1} related to $E^{(1)}_{1g}$, E_{2g}, $E^{(2)}_{1g}$, $A^{(1)}_{1g}$, $E^{(2)}_{1g}$, and $A^{(2)}_{1g}$ modes, respectively (Figure S5b).[18] These modes are due to shear and longitudinal vibrations of Ti and Al atoms, where the E_{1g} (128.3 cm^{-1}) mode

is characteristic of Al.[19] Post-etching treatment involves the disappearance of older bands while new upshifted Raman bands appear, confirming the successful removal of Al and the formation of surface terminations on the MXenes. The Raman spectra of MXenes after etching are segregated into three regions: the lower frequency region (flake region) involving in-plane and out-of-plane Raman modes of the Ti atom vis-a-vis C backbone (100-170 cm^{-1}), the intermediate region (functional group region) that involves the vibrational modes of surface terminations, and the carbon region which involves the in-plane and out-of- plane vibrations of C atoms vis-à-vis Ti backbone.

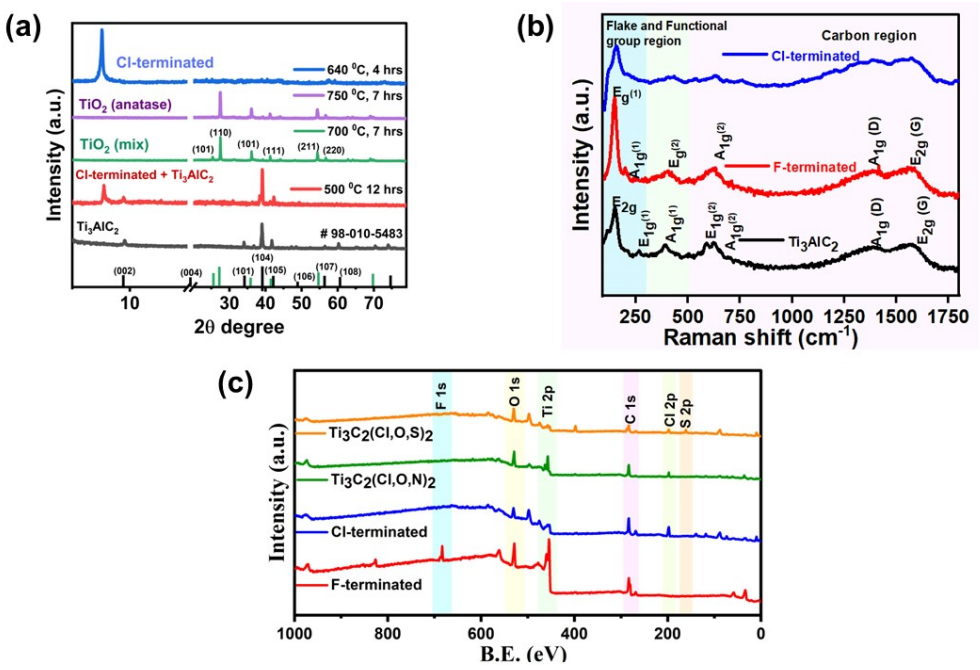

Figure S5: ***(a)*** *PXRD depicting optimized synthesis of Cl-terminated MXene,* ***(b)*** *Raman spectra showing characteristic functional groups and carbon regions of* Ti_3AlC_2 *and functionalized Cl-terminated MXenes, and* ***(c)*** *survey spectra of all the MXenes.*

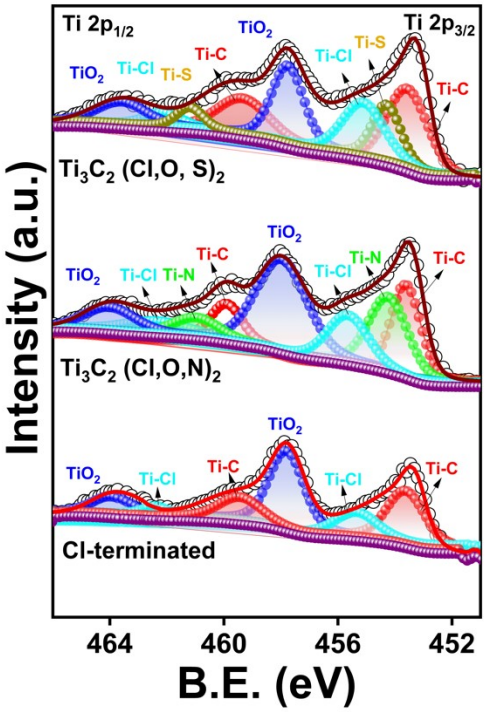

Figure S6: CL-XPS of Ti 2p for Ti_3C_2 (Cl, O)$_2$, Ti_3C_2 (Cl, O, N)$_2$ and Ti_3C_2 (Cl, O, S)$_2$

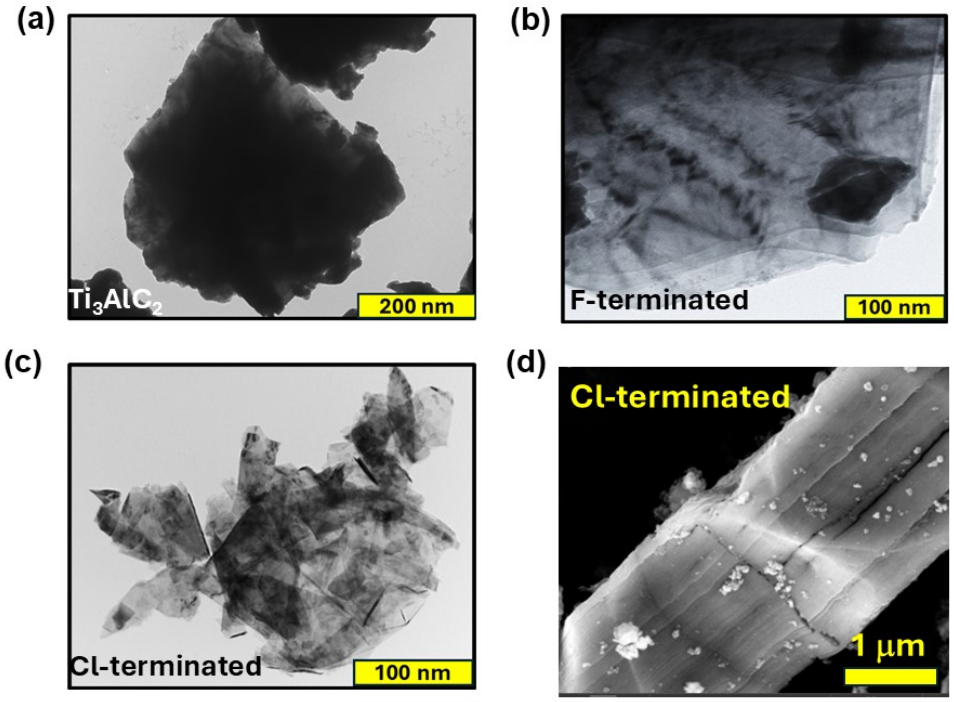

Figure S7: *TEM images depicting layered morphology of* ***(a)*** *Ti_3AlC_2,* ***(b)*** *F-terminated, and* ***(c)*** *Cl-terminated MXenes because of chemical etching and delamination, and* ***(d)*** *SEM image of Cl-terminated MXene showing the layered morphology.*

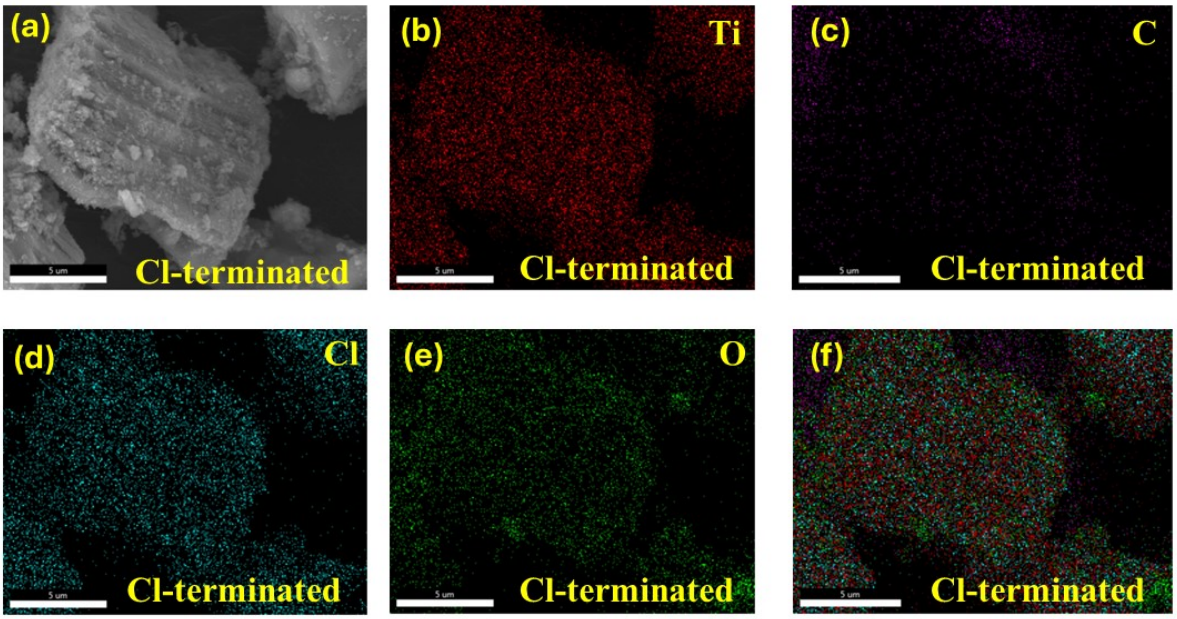

Figure S8: ***(a)*** *SEM image of Cl-terminated MXene, and* ***(b-e)*** *elemental distribution showing the uniform distribution of Ti, C, Cl, and O, and for all the elements* ***(f)****.*

(a)

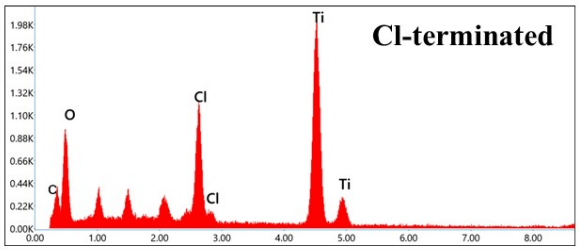

(b)

Element	Weight %	Atomic %
C K	16.8	28.5
O K	28.1	43.0
Cl K	10.6	6.9
Ti K	44.5	21.6

Figure S9: ***(a)*** *Elemental mapping showing the presence of elements Ti, C, Cl, and O and* ***(b)*** *Table of atomic and weight percentages for Cl-terminated MXene.*

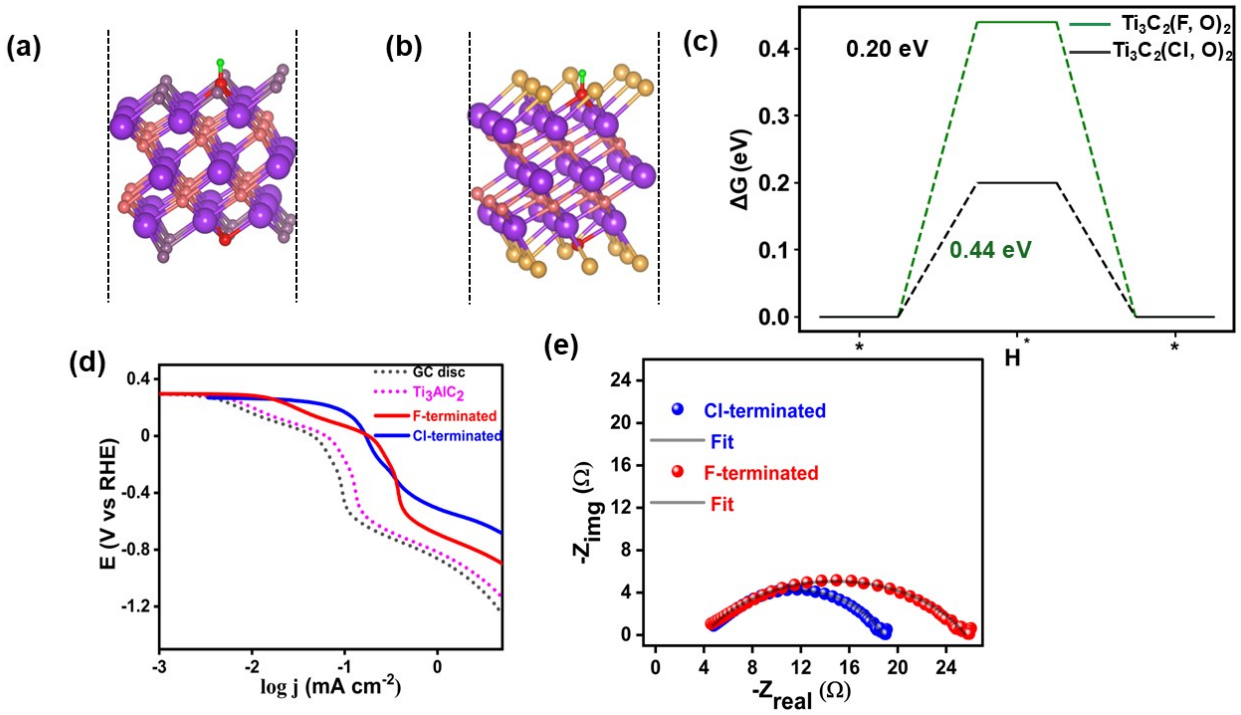

Figure S10: *The optimized geometries of O-substituted* ***(a)*** *$Ti_3C_2F_2$,* ***(b)*** *$Ti_3C_2Cl_2$ MXenes.* ***(c)*** *The Gibbs free energy profile for hydrogen adsorption on $Ti_3C_2(F,O)$ and $Ti_3C_2(Cl,O)$ MXenes.* ***(d)*** *Tafel plots showing the variation of E v/s log j* ***(e)*** *(Nyquist) EIS taken at -0.8 V vs RHE in the frequency range of 20 KHz to 0.1 Hz with a perturbation amplitude of 0.005 V_{RMS}, showing the fitted (line) and real data (points).*

Table S2: The EIS parameters solution resistance (R_s), charge transfer resistance (R_{ct}), and double layer capacitance (C_{dl}) estimated from the fitting of Nyquist plots (Figure S10e).

Catalyst	**R_s (ohm)**	**R_{ct} (ohm)**
F-terminated	4.78	21.13
Cl-terminated	4.79	14.21

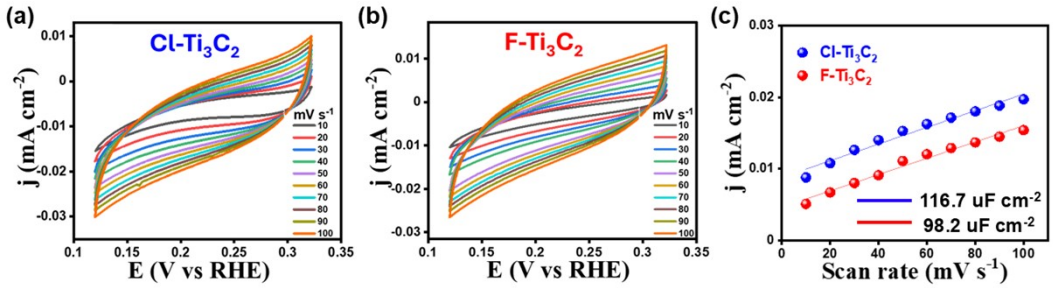

Figure S11: (a, b) *CV taken at different scan rates (10-100 mV s^{-1}) in 0.05 M H_2SO_4 in the capacitive potential region (0.1-0.35 V vs RHE) for Cl-Ti_3C_2 and F-Ti_3C_2 MXenes for determining the ECSA, and* ***(c)*** *linear plot of j (mA cm^{-2}) vs scan rate (mV s^{-1}) to estimate the double layer capacitance (directly proportional to the ECSA) from the slope.*

Section S7:Solvent effect

We employed VASPsol, a software package integrating solvation effects within VASP using a self-consistent continuum model for implicit solvation calculations.[20] VASPsol has gained popularity recently due to its computational efficiency and simplicity, making it a valuable tool for studying various heterogeneous catalysis systems.[21,22] In this approach, the total energy obtained from DFT is supplemented by contributions from electrostatic interactions between the solute and solvent and the cavitation energy required to form the solute within the solvent environment. The following equation gives the expression for E_{elec} and E_{cav}:

$$E_{cav} = \tau \int d\vec{r} |\nabla S(\vec{r})| \quad (1)$$

$$E_{elec} = - \int d\vec{r} \varepsilon(\vec{r}) \frac{|\nabla \phi(\vec{r})|^2}{8\pi} \quad (2)$$

where, $\varepsilon(\vec{r})$ represents the solvent dielectric constant, $S(\vec{r})$ is the cavity shape function, $\phi(\vec{r})$ is the total electrostatic potential, and τ is the surface tension. The dielectric constant and cavity shape function are given by:

$$\varepsilon\left(n_{\text{solute}}(\vec{r})\right) = 1 + (\varepsilon_b - 1) S\left(n_{\text{solute}}(\vec{r})\right) \quad (3)$$

$$S(r) = \frac{1}{2}\text{erfc}\left\{\frac{\ln\left(\rho(r)/\rho_c\right)}{\sigma\sqrt{2}}\right\} \quad (4)$$

where ρ is the electron density, ρ_c is the cutoff electron density, and σ defines the cavity width.

In our simulations, aqueous solvation was modeled using a bulk dielectric constant $\varepsilon_b = 78.35$represent water, consistent with experimental conditions. The electrolyte screening effect was included through a Debye length (λ_D) of 3.0 Å, capturing ionic strength-induced potential decay near the solid-liquid interface.[23] Other solvation parameters were set to standard values.

Section S8: 2p Non-Metal Substitution

The substitution energy is calculated by randomly substituting a 2*p* non-metal with a -Cl atom using the following formula:

$$G_{sub} = H(Cl_{8/9}T'_{1/9})_{substituted} - H(Ti_3C_2T_2)_{pure} + \mu_{Cl} - \mu_{non\text{-}metal(T')}$$

where $H(Cl_{8/9}T'_{1/9})_{substituted}$ is the energy of the non-metal substituted system and $H(Ti_3C_2T_2)_{pure}$ is the energy of the pure system, μ_{Cl} and $\mu_{non\text{-}metal(T')}$ is the chemical potential of Cl and non-metal T' calculated using[24]:

$$\mu_{Cl}(p_0, T) = \tfrac{1}{2} G_{Cl2}$$

$$\mu_{T'}(p_0, T) = \tfrac{1}{2} G_{T'2}$$

where G_{X2} and $G_{T'2}$ are the gas-phase free energy of the diatomic molecule and 2*p* non-metal at standard conditions.

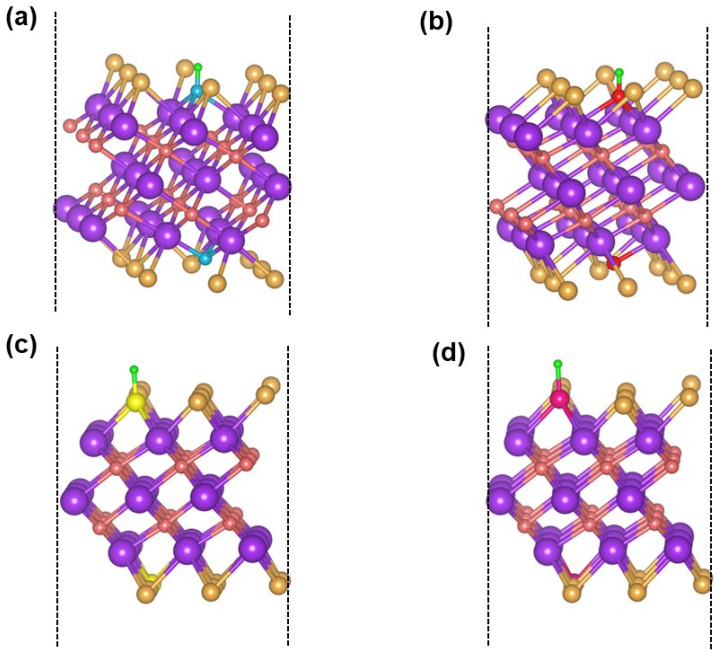

Figure S12: *Top view of chemical structures reaction intermediates for H adsorbed on the* ***(a)*** *$Ti_3C_2(Cl, N)_2$,* ***(b)*** *$Ti_3C_2(Cl, O)_2$,* ***(c)*** *$Ti_3C_2(Cl, S)_2$, and* ***(d)*** *$Ti_3C_2(Cl, Se)_2$, MXenes.*

Section S9: Impact of non-metal Configuration and Concentration on HER Performance

From n_x=1 to n_x=2, we observe that -O terminations preferentially occupy neighboring sites (positions 1 and 2) coordinated to the same Ti center, rather than being spatially separated. When the two -O atoms are in close proximity, ΔG_{H^*} on the O-top site is significantly reduced to 0.12 eV. In contrast, when these atoms are placed farther apart, ΔG_{H^*} increases to 0.19 eV, indicating less favorable hydrogen adsorption. This demonstrates that spatial proximity enables synergistic electronic effects between neighboring O atoms, effectively tuning the local electronic environment to enhance HER activity. Hence, at higher non-metal concentration (n_x =2), O prefers to share a common Ti centre, with adjacent O atoms (positions 1 and 2) exhibiting higher HER activity than when positioned separately. Similarly, for S and Se substitutions at n_x =2, ΔG_{H^*} decreases by approximately 16.4% and 19.0%, respectively, compared to n_x=1, further underscoring the role of dopant proximity in promoting catalytic efficiency. The indices on the O atom in Figure S10a indicate nearest and second-nearest substitution. The left panel shows when two oxygen atoms are at their nearest, and the right panel shows the far-away substitution. The Gibbs free energy profile at higher dopant concentration (n_x =2) is shown in Figure S11.

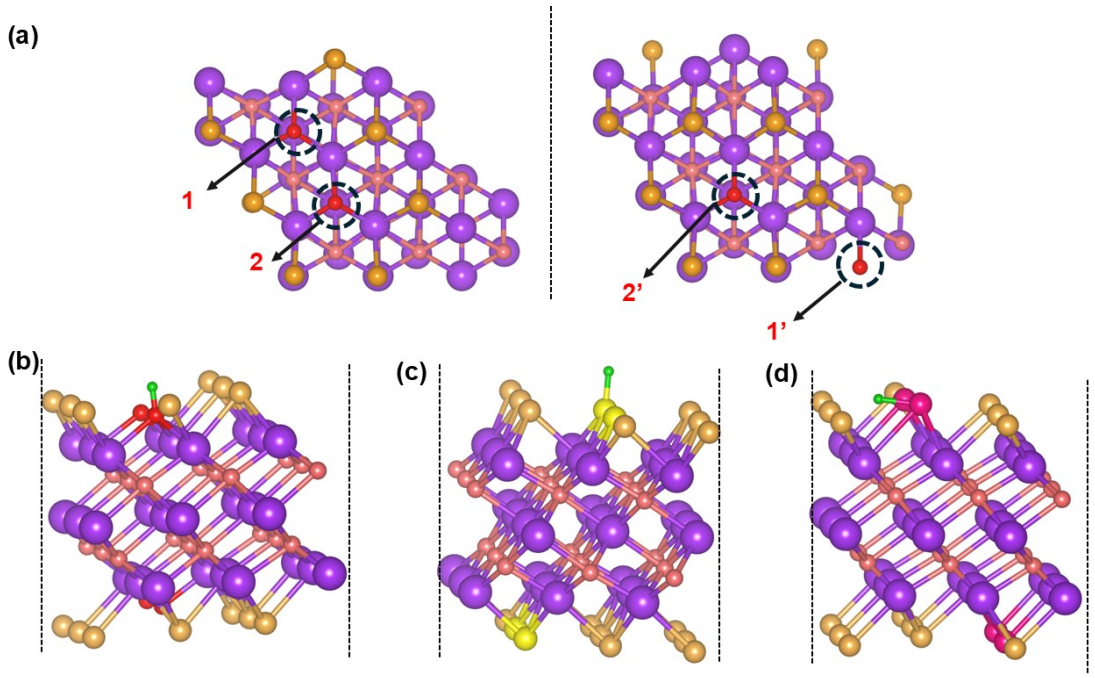

Figure S13: ***(a)*** *The optimized geometries$Ti_3C_2(Cl, O)_2$ at n_x=2, when substituted nearly (left panel) and far way (right panel), Top view of chemical structures reaction intermediates for H*

adsorbed on the ***(b)*** *$Ti_3C_2(Cl, O)_2$,* ***(c)*** *$Ti_3C_2(Cl, S)_2$,* ***(d)*** *$Ti_3C_2(Cl, Se)_2$ at higher dopant concentration (n_x =2 per layer)*

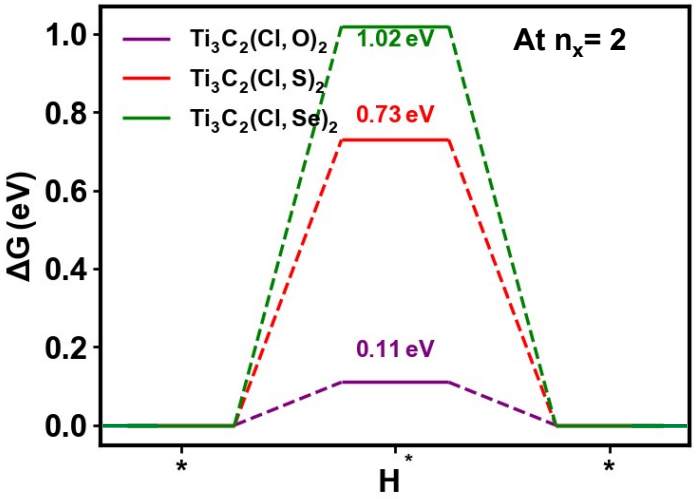

Figure S14: *Gibbs free energy (ΔG_{H^*}) diagrams for $Ti_3C_2(Cl, T')_2$ MXenes (T" = O, S, and Se) at higher dopant concentration of n_x =2 per layer.*

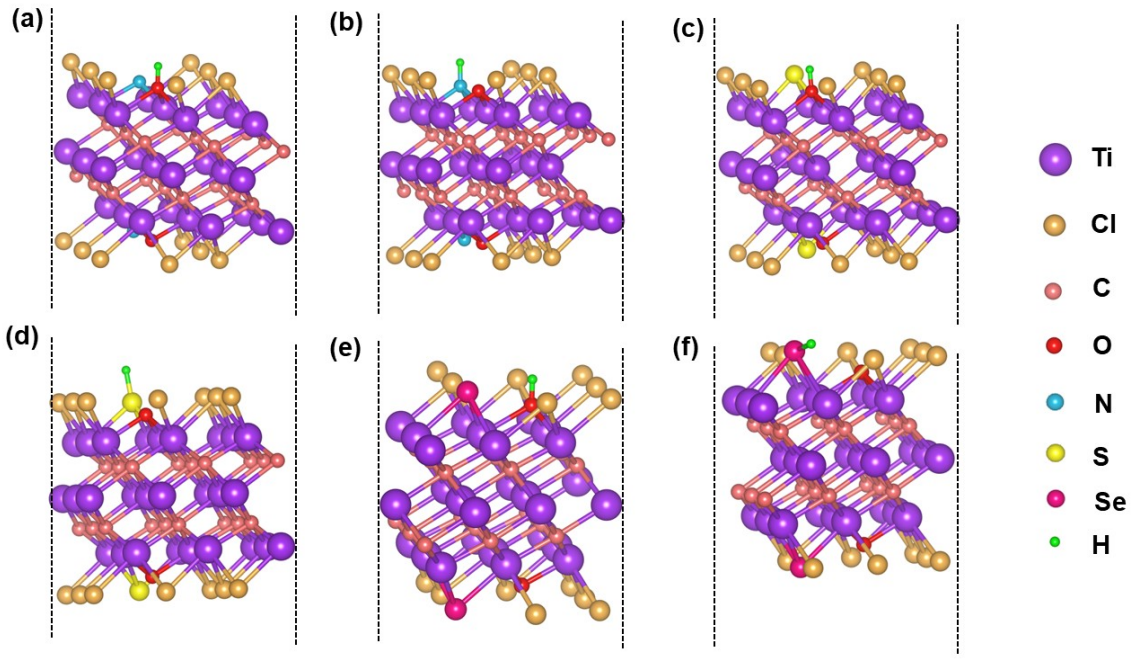

Figure S15: *Top view of chemical structures reaction intermediates for H adsorbed on the* ***(a)*** *Ti_3C_2(Cl, O, N)$_2$: (O-top),* ***(b)*** *Ti_3C_2(Cl, O, N)$_2$: (N-top),* ***(c)*** *Ti_3C_2(Cl, O, S)$_2$: (O-top),* ***(d)*** *Ti_3C_2(Cl, O, S)$_2$: (S-top),* ***(e)*** *Ti_3C_2(Cl, O, Se)$_2$: (O-top), and* ***(f)*** *Ti_3C_2(Cl, O, Se)$_2$: (Se-top).*

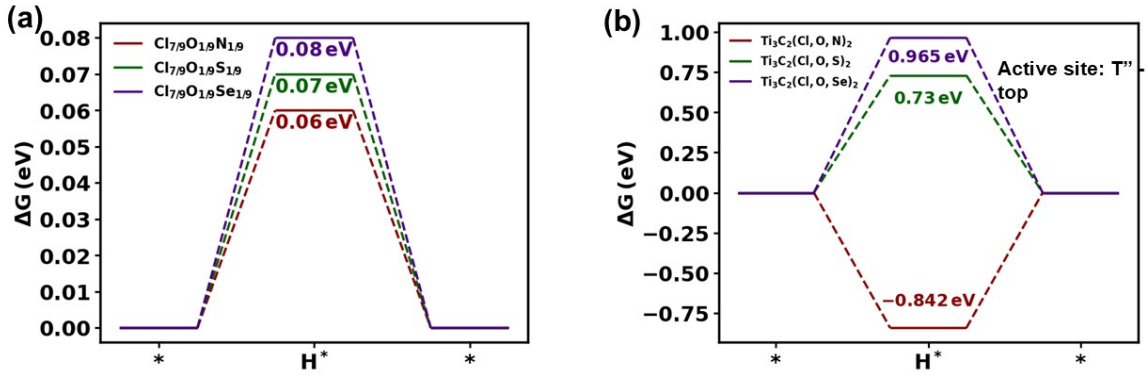

Figure S16: ***(a)*** *Gibbs free energy profile for non-metal substituted ternary configuration MXenes (n_x=1 (O) and n_y=1 (N, S, Se).* ***(b)*** *Gibbs free energy (ΔG_{H^*}) diagrams for Ti_3C_2(Cl, O, T'')$_2$MXenes (T'' = N, S, and Se) on N-top, S-top, and Se-top.*

Section S10: Synthesis and Characterization of Ti_3C_2(Cl, O, N)$_2$ and Ti_3C_2(Cl, O, S)$_2$MXenes

Specifically, the as-synthesized Cl-Ti_3C_2 was dispersed in 20 mL of ethylenediamine (EDA) for nitrogen substitution and in 20 mL of carbon disulfide (CS_2) for S substitution. The reaction was carried out under hydrothermal conditions at 120°C for 12 hours, facilitating the incorporation of N and S atoms into the MXene structure via surface functionalization.[25,26] The reaction mixtures were thoroughly washed with distilled water to remove unreacted precursors and the by-products. The purified N-Cl-Ti_3C_2 and S-Cl-Ti_3C_2 powders were then dried in a vacuum oven at 60°C for 12 hours to eliminate residual moisture. To preserve the structural integrity and prevent unwanted surface oxidation, the samples were subsequently stored under vacuum conditions for further analysis.

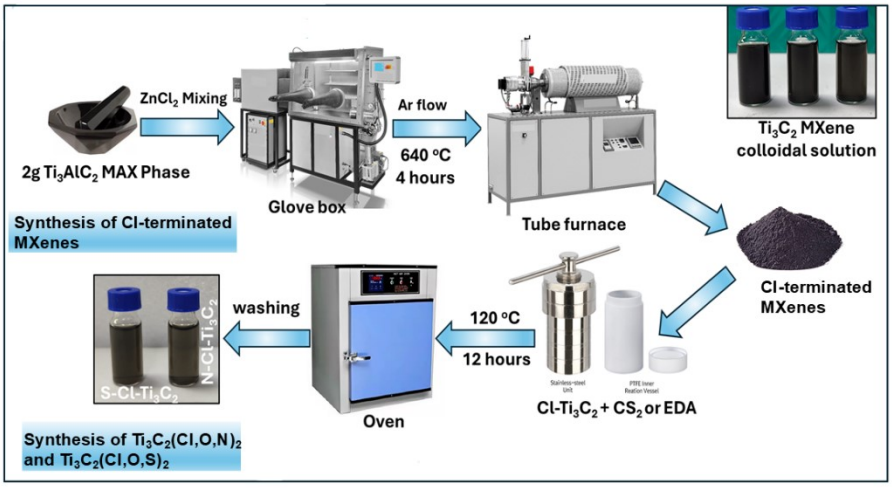

Scheme 2: A detailed protocol was followed for the synthesis of $Ti_3C_2(Cl, O, N)_2$ and $Ti_3C_2(Cl, O, S)_2$ MXenes using chemical HF etching, molten $ZnCl_2$ salt etching, and hydrothermal treatment, respectively.

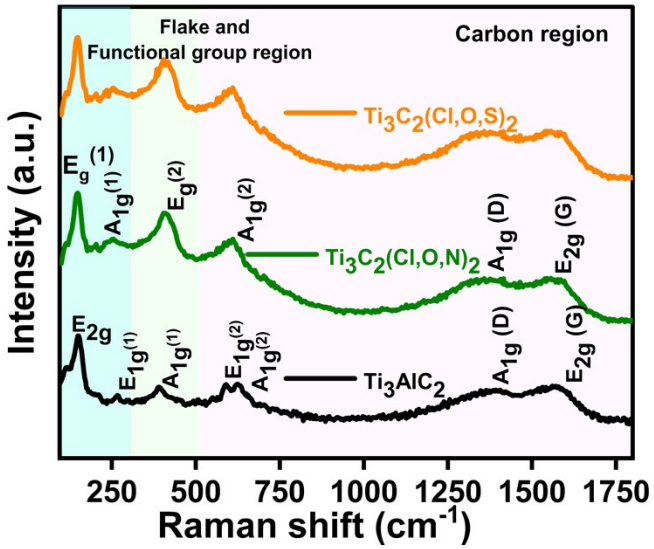

Figure S17: *Raman spectra showing characteristic functional groups and carbon regions of Ti_3AlC_2 and functionalized -N and* -S functionalized *Cl-terminated MXenes.*

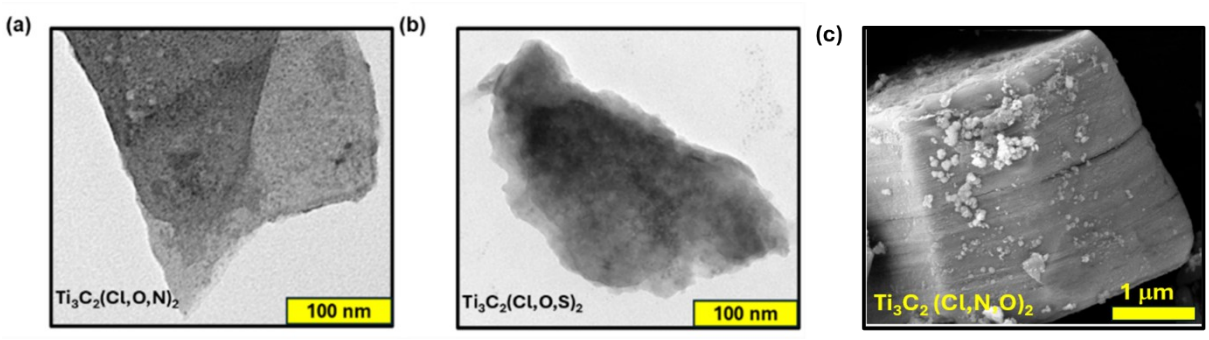

Figure S18: ***(a-c)*** *TEM images depicting layered morphology of* ***(a)*** $Ti_3C_2(Cl, O, N)_2$, ***(b)*** $Ti_3C_2(Cl, O, S)_2$ *MXenes as a result of chemical etching and delamination and (c) SEM image of* $Ti_3C_2(Cl, O, N)_2$ *MXene.*

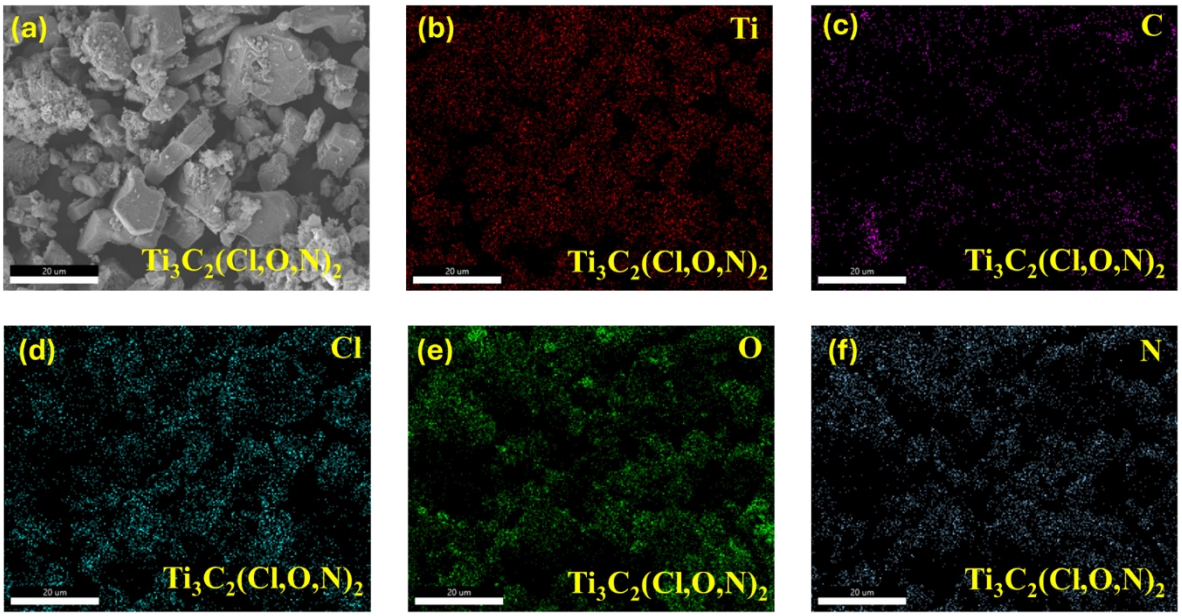

Figure S19: *(a) SEM image of* $Ti_3C_2(Cl, O, N)_2$ *MXene and Elemental distribution of* ***(b-f)*** $Ti_3C_2(Cl,O,N)_2$ *showing layered morphology and presence of Ti, C, O, Cl, and N.*

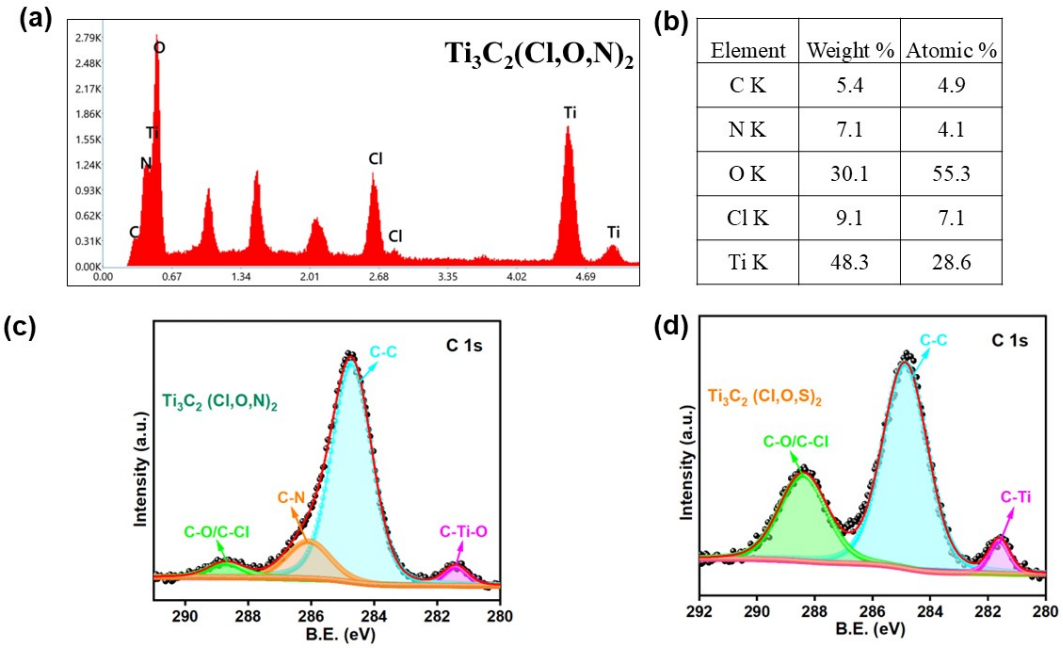

Element	Weight %	Atomic %
C K	5.4	4.9
N K	7.1	4.1
O K	30.1	55.3
Cl K	9.1	7.1
Ti K	48.3	28.6

Figure S20: (a) elemental mapping showing the presence of elements Ti, C, Cl, and O and (b) table of atomic and weight percentages for Cl-terminated MXene. *CL XPS spectra of* ***(c)*** *C 1s for* $Ti_3C_2(Cl, O, N)_2$, *and* ***(d)*** *C 1s for* $Ti_3C_2(Cl, O, S)_2$ *MXene.*

Table S3: *Quantitative Analysis of survey XPS spectra:*

Catalysts	**Atomic %**					
	N	S	O	C	Cl	Ti
$Ti_3C_2(O,Cl)_2$	-	-	34.86	36.74	10.2	18.2
$Ti_3C_2(N,Cl)_2$	6.2	-	44.14	15.8	9.8	24.06
$Ti_3C_2(S,Cl)_2$	-	5.9	32.49	31.44	9.72	20.45

Table S4: *EDS and ICP analysis.*

Sample	**Precursor concentration**	**ICP (mol%)**					**EDS (mol%)**				
	(%N)	Ti	C	O	Cl	N	Ti	C	O	Cl	N
Cl-Ti_3C_2	0	0.97	0.97	1.68	0.34	-	0.93	0.99	1.75	0.31	-
N*-Cl-Ti_3C_2	2	1.2	0.75	1.71	0.29	0.41	1.19	0.81	1.80	0.24	0.40
N$^{\#}$-Cl-Ti_3C_2	4	1.1	0.71	1.75	0.32	0.49	1.07	0.76	1.84	0.26	0.46
N-Cl-Ti_3C_2	6	1.05	0.69	1.79	0.31	0.54	1.01	0.70	1.88	0.26	0.50

N°-Cl-Ti_3C_2	8	1.07	0.70	1.76	0.29	0.57	1.0	0.72	1.86	0.25	0.56

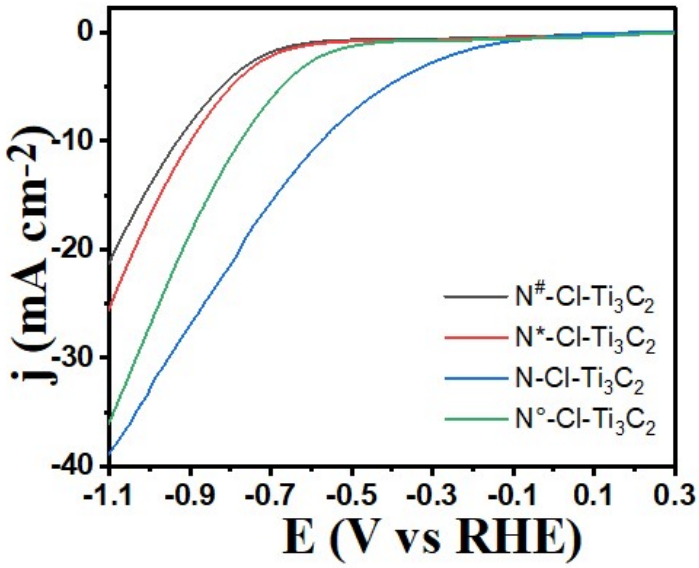

Figure S21: *LSV curves for different doping concentrations for N-Cl-Ti_3C_2.*

Table S5: *The EIS parameters solution resistance (R_s), charge transfer resistance (R_{ct}), and double layer capacitance (C_{dl}) estimated from the fitting of Nyquist plots (Figure 6c)*

Catalyst	R_s (ohm)	R_{ct} (ohm)
N-Cl-Ti_3C_2	4.99	7.83
S-Cl-Ti_3C_2	4.99	11.71

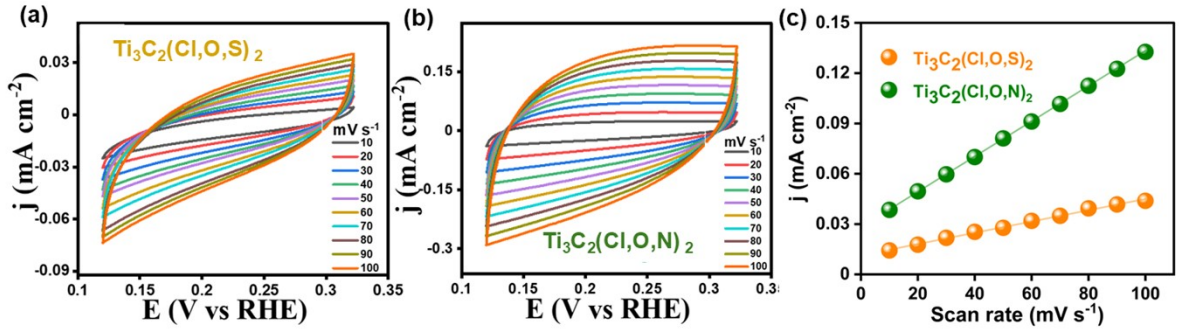

Figure S22: (a, b) *CV taken at different scan rates (10-100 mV s^{-1}) in 0.05 M H_2SO_4 in the capacitive potential region (0.1-0.4 V vs RHE) for Ti_3C_2(Cl, O, S)$_2$ and Ti_3C_2(Cl, O, N)$_2$*

MXenes for determining the ECSA, and ***(c)*** *linear plot of j (mA cm^{-2}) vs scan rate (mV s^{-1}) to estimate the double layer capacitance (directly proportional to the ECSA) from the slope.*

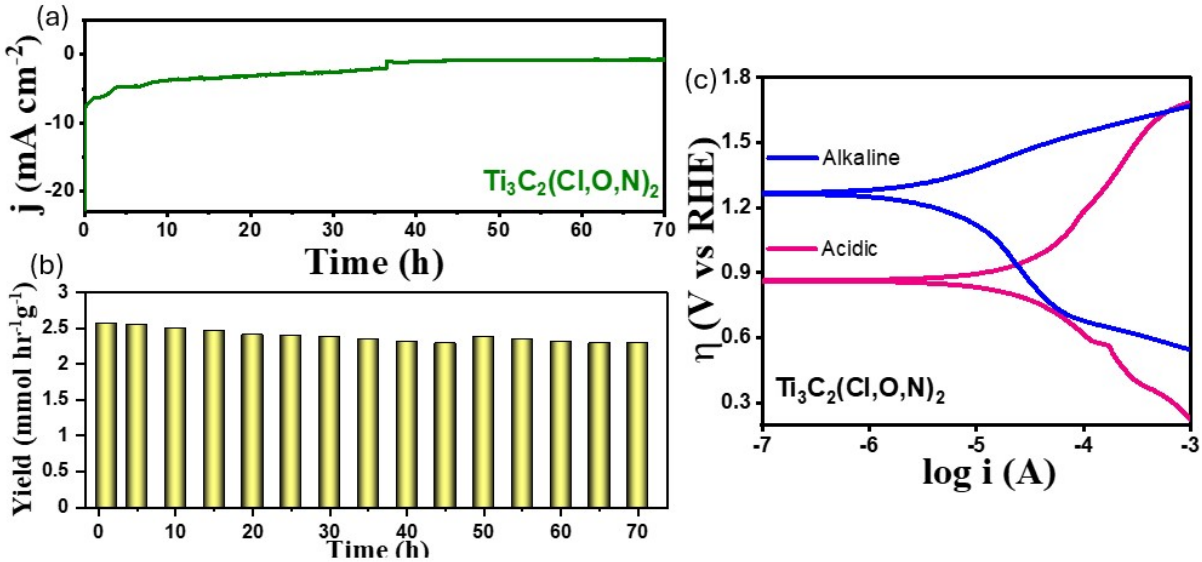

Figure S23: (a) *CA at -0.5 V vs RHE in 0.05 M H_2SO_4 taken for 70 hours,* ***(b)*** *catalyst performance in terms of hydrogen production rate, and* ***(c)*** *E vs log i showing the corrosion potential and corrosion resistance of Ti_3C_2 (Cl, O, N)$_2$ MXene in acidic and alkaline conditions.*

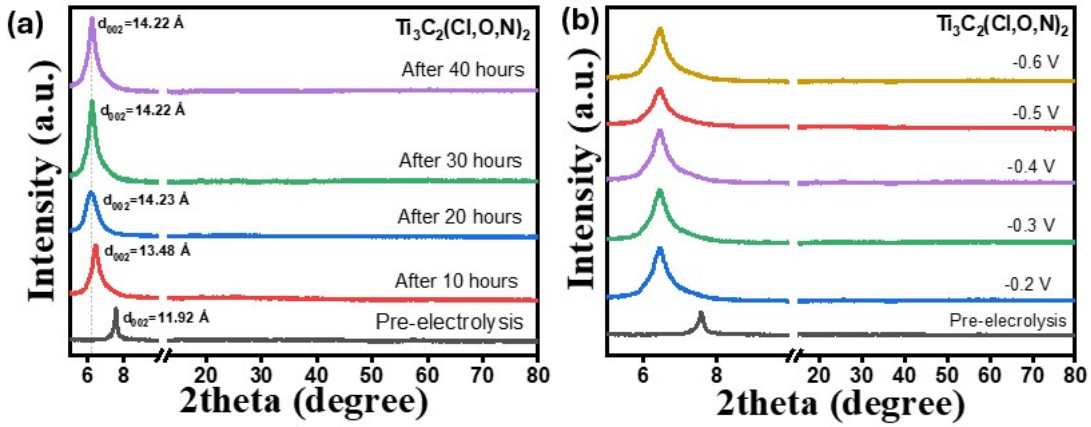

Figure S24: post-electrolysis XRD of Ti_3C_2 (Cl, O, N)$_2$ MXene after various electrolysis hours (a) and at various applied potentials showing no appreciable change in the (002) plane.

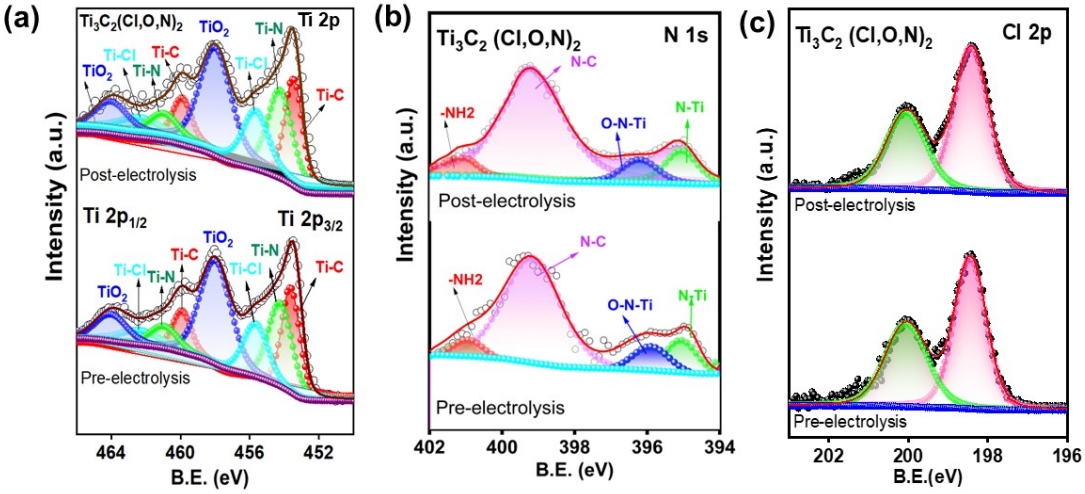

Figure S25: Pre- and post-electrolysis CL-XPS of Ti 2p (a), N 1s, (b) and Cl 2p (c) for Ti_3C_2 (Cl, O, N)$_2$ MXene after 70 hours of electrolysis.

Section S11: Spearman's rank correlation matrices

The structural properties, including nearest neighbor bond length, bond angle, active site (A.S)-Ti bond length, A.S-H bond distance, and electronic features such as a charge on the active site and *p*-band center, are crucial indicators governing the HER activity of the non-metal doped system.[27,28] All the structural descriptors are extracted using a nearest-neighbor threshold of 5 Å.

Table S6: *The detailed description of selected descriptors.*

Features	Description
dA.S-Ti(9′)	Change in bond length between active site (A.S) and Ti atom (9) before and after H adsorption in the *np* non-metal substituted systems. (Inset in Figure 7a)
dA.S-Ti(12′)	Change in bond length between active site (A.S) and Ti atom (12) before and after H adsorption in the *np* non-metal substituted systems.
$\langle d_{near} \rangle$(H)	Average of the change in the nearest neighbor bond lengths on hydrogen adsorption with respect to (w.r.t) the np non-

	metal substituted systems.
dA.S-Ti(9)	Change in bond length between active site (A.S) and Ti atom (9) on substitution w.r.t the pristine $Ti_3C_2Cl_2$ system.
dA.S-Ti(10)	Change in bond length between active site (A.S) and Ti atom (10) on substitution w.r.t the pristine $Ti_3C_2Cl_2$ system.
∠Ti(9')-A.S-Ti(12')	Change in the bond angle between Ti(9'), A.S, and Ti(12') atoms after H adsorption w.r.t the substituted system.
∠Ti(12')-A.S-Ti(13')	Change in the bond angle between Ti(12'), A.S, and Ti(13') atoms after H adsorption w.r.t the substituted system.
∠Ti(13)-A.S-Ti(10)	Change in the bond angle between Ti(13), A.S, and Ti(10) atoms in the substituted system w.r.t the pristine $Ti_3C_2Cl_2$ system.
Voronoi_vol(A.S)	Voronoi volume of the active site atom, representing local atomic packing density.
⟨d(A.S-Ti)⟩	Average A.S-Ti bond distance in the substituted system
Voronoi(diff)	Change in Voronoi volume of the active site in the substituted system w.r.t the pristine system.
qA.S	Bader charge on the active site atom.
qnear(A.S)	Total Bader charge on atoms neighboring the active site.
⟨qTi⟩	The average Bader charge on Ti atoms in the system in the substituted systems.
Δ<qTi−qTi′>	Change in average Ti charge before vs. after H adsorption in the substituted systems.
<qA.S−qA.S′)	Change in A.S charge before vs. after H adsorption

p-band center	p-band center of the active site atom.
Total_Surface_q	Total Bader charge on the exposed surface atoms

The detailed descriptions of various structural and electronic features are incorporated in Section S11. All the features were carefully selected to capture the local structural and electronic features, such as changes in the nearest neighbor bond lengths, bond angles (with respect to the pristine $Ti_3C_2Cl_2$ system), changes in nearest neighbor bond length and angles after hydrogen adsorption in the *np* non-metal substituted system, site-specific Bader charge, and total charge on the surface. To enhance structural representability, additional geometric descriptors, such as Voronoi volume, bond-length statistics (mean, standard deviation, and extrema), and distortion indices, were incorporated. The electronic domain was expanded to include the d-band center and d-band difference. The highly correlated features with a threshold value set at ≥ 0.95 were excluded from the structural and electronic datasets based on their linear and nonlinear correlations using Pearson and Spearman correlation matrices. These redundant variables were excluded, yielding a refined dataset with 15 configurations and 18 non-redundant features.

Interdependence Between Structural and Electronic Descriptors:

The strong interdependence between the geometric descriptor $d_{A.S\text{-}Ti(9)}$ and the electronic descriptor $q_{A.S}$ underlies the observed variation in ΔG_H across the *np* non-metal substituted $Ti_3C_2Cl_2$ MXenes. This relationship arises because substitution of O, N, S or Se exerts a *chemical pressure* by replacing the larger, weakly electronegative Cl atoms at the surface, which locally contracts the Ti-A.S bond and enhances charge localization at the active site. Consequently, smaller and more electronegative dopants (O, N) induce stronger bond contraction and greater charge accumulation, while larger and less electronegative dopants (S, Se) result in weaker perturbations.

The strong negative correlation ($\rho = -0.94$) between $q_{A.S}$ and $d_{A.S\text{-}Ti(9)}$ as shown in Figure 7a indicates that as the Ti-A.S bond contracts, charge accumulates on the non-metal active site, thereby strengthening H* adsorption (more negative ΔG_H). However, this relationship is nonlinear: excessive bond contraction or charge accumulation leads to overbinding ($\Delta G_H \ll 0$), ultimately hindering hydrogen desorption.

Therefore, $d_{A.S\text{-}Ti(9)}$ descriptor simultaneously captures the effects of local coordination distortion and electronic charge redistribution induced by non-metal substitution. The optimal

catalytic regime is achieved when both parameters reach a balanced range consistent with the Sabatier principle, where H* adsorption and desorption are thermodynamically balanced ($\Delta G_H \approx 0$).

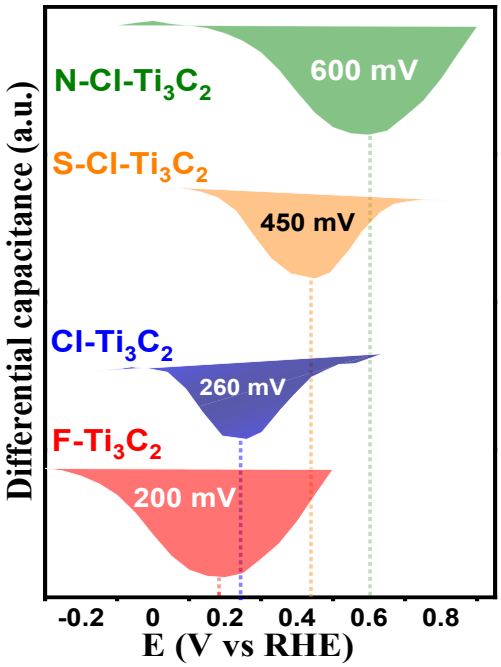

Figure S26: *Overlay of the differential capacitance curves estimated from the Mott-Schottky measurements performed at a frequency of 1000 Hz with a sinusoidal perturbation amplitude of 0.005 V to estimate the potential of zero charge (E_{PZC}) for the utilized MXene materials.*

Table S7: The State-of-the-art catalysts and corresponding references.

HER catalyst	Electrolyte	Tafel slope	References
$MoSe_2$@Ti-MXene	0.5 M H_2SO_4	91 mV/dec	[29]
$Ti_3CN(OH)_x$@MoS_2	0.5 M H_2SO_4	64 mV/dec	[30]
Ti_2CT_x	0.5 M H_2SO_4	100 mV/dec	[31]
Mo_2CT_x	0.5 M H_2SO_4	82 mV/dec	[32]
Ti_2CT_x	0.5 M H_2SO_4	124 mV/dec	[32]
$Ti_3C_2T_x$	0.5 M H_2SO_4	97 mV/dec	[33]
MoS_2@$Ti_3C_2T_x$	0.5 M H_2SO_4	70 mV/dec	[34]
NiS_2/V_2CT_x	1.0 M KOH	85 mV/dec	[35]
Ti_3C_2 (Cl, O, N)$_2$	**0.05 M H_2SO_4**	**68 mV/dec**	**This work**

References:

(1) Li, M.; Li, X.; Qin, G.; Luo, K.; Lu, J.; Li, Y.; Liang, G.; Huang, Z.; Hultman, L.; Eklund, P.; Persson, P. O. A.; Du, S.; Chai, Z.; Zhi, C.; Huang, Q. Halogenated MXenes with Electrochemically Active Terminals for High Performance Zinc Ion Batteries. **2020**.

(2) Dahlqvist, M.; Rosen, J. Chalcogen and Halogen Surface Termination Coverage in MXenes—Structure, Stability, and Properties. *NPJ 2D Mater Appl* **2024**, *8* (1), 65. https://doi.org/10.1038/s41699-024-00502-8.

(3) Bagheri, M.; Ibragimova, R.; Komsa, H.-P. Fermiology of Two-Dimensional Titanium Carbide and Nitride MXenes. *Phys Rev B* **2021**, *104* (3), 035408. https://doi.org/10.1103/PhysRevB.104.035408.

(4) Teli, A. M.; Mane, S. M.; Mishra, R. K.; Jeon, W.; Shin, J. C. Unlocking the Potential of Ti3C2Tx MXene: Present Trends and Future Developments of Gas Sensing. *Micromachines (Basel)* **2025**, *16* (2), 159. https://doi.org/10.3390/mi16020159.

(5) Savin, A.; Jepsen, O.; Flad, J.; Andersen, O. K.; Preuss, H.; von Schnering, H. G. Electron Localization in Solid-State Structures of the Elements: The Diamond Structure. *Angewandte Chemie International Edition in English* **1992**, *31* (2), 187–188. https://doi.org/10.1002/anie.199201871.

(6) Becke, A. D.; Edgecombe, K. E. A Simple Measure of Electron Localization in Atomic and Molecular Systems. *J Chem Phys* **1990**, *92* (9), 5397–5403. https://doi.org/10.1063/1.458517.

(7) Koumpouras, K.; Larsson, J. A. Distinguishing between Chemical Bonding and Physical Binding Using Electron Localization Function (ELF). *Journal of Physics: Condensed Matter* **2020**, *32* (31), 315502. https://doi.org/10.1088/1361-648X/ab7fd8.

(8) Kemppainen, E.; Halme, J.; Lund, P. D. An Analytical Model of Hydrogen Evolution and Oxidation Reactions on Electrodes Partially Covered with a Catalyst. *Physical Chemistry Chemical Physics* **2016**, *18* (19), 13616–13628. https://doi.org/10.1039/C6CP00908E.

(9) Khatun, S.; Hirani, H.; Roy, P. Seawater Electrocatalysis: Activity and Selectivity. *J Mater Chem A Mater* **2021**, *9* (1), 74–86. https://doi.org/10.1039/D0TA08709B.

(10) Kumari, A.; Ghosh, D. Fast Carrier Recombination, Nanoconfinement, and Defects Boost Solar-Driven Hydrogen Evolution Reactions at Z-Scheme Heterojunctions. *ACS Appl Energy Mater* **2024**, *7* (20), 9460–9469. https://doi.org/10.1021/acsaem.4c02101.

(11) Zhu, L.; Ji, J.; Yin, H.; Zhao, H. Pseudocapacitance of Cl-Terminated MXene Nanosheets for Efficient Chloride-Ion Hybrid Capacitors. *Energy & Fuels* **2023**, *37* (7), 5607–5612. https://doi.org/10.1021/acs.energyfuels.3c00248.

(12) Bhat, A. Y.; Bashir, A. U.; Jain, P.; Bhat, M. A.; Ingole, P. P. Unraveling the Active Sites on Mesoporous $CuFe_2O_4$@N-Carbon Catalysts with Abundant Oxygen Vacancies and M-N-C Content for Boosted Nitrogen Reduction Toward Electrosynthesis of Ammonia. *Small* **2024**, *20* (45). https://doi.org/10.1002/smll.202403319.

(13) Alhabeb, M.; Maleski, K.; Anasori, B.; Lelyukh, P.; Clark, L.; Sin, S.; Gogotsi, Y. Guidelines for Synthesis and Processing of Two-Dimensional Titanium Carbide ($Ti_3C_2T_x$ MXene). *Chemistry of Materials* **2017**, *29* (18), 7633–7644. https://doi.org/10.1021/acs.chemmater.7b02847.

(14) Gao, X.; Gao, K.; Zhu, W.; Liang, C.; Li, Q.; Fu, F.; Zhu, Y. Accurate Guided Alternating Atomic Layer Enhance Internal Electric Field to Steering Photogenerated Charge Separation for Enhance Photocatalytic Activity. *Appl Catal B* **2021**, *298*. https://doi.org/10.1016/j.apcatb.2021.120536.

(15) Parker, T.; Zhang, D.; Bugallo, D.; Shevchuk, K.; Downes, M.; Valurouthu, G.; Inman, A.; Chacon, B.; Zhang, T.; Shuck, C. E.; Hu, Y.-J.; Gogotsi, Y. Fourier-Transform Infrared Spectral Library of MXenes. *Chemistry of Materials* **2024**, *36* (17), 8437–8446. https://doi.org/10.1021/acs.chemmater.4c01536.

(16) Zhou, B.; Zhang, Z.; Li, Y.; Han, G.; Feng, Y.; Wang, B.; Zhang, D.; Ma, J.; Liu, C. Flexible, Robust, and Multifunctional Electromagnetic Interference Shielding Film with Alternating Cellulose Nanofiber and MXene Layers. *ACS Appl Mater Interfaces* **2020**, *12* (4), 4895–4905. https://doi.org/10.1021/acsami.9b19768.

(17) Yang, F.; Hegh, D.; Song, D.; Zhang, J.; Usman, K. A. S.; Liu, C.; Wang, Z.; Ma, W.; Yang, W.; Qin, S.; Razal, J. M. Synthesis of Nitrogen-Sulfur Co-Doped Ti3C2T MXene with Enhanced Electrochemical Properties. *Materials Reports: Energy* **2022**, *2* (1), 100079. https://doi.org/10.1016/j.matre.2022.100079.

(18) Presser, V.; Naguib, M.; Chaput, L.; Togo, A.; Hug, G.; Barsoum, M. W. First-order Raman Scattering of the MAX Phases: Ti_2AlN, $Ti_2AlC_{0.5}N_{0.5}$, Ti_2AlC, $(Ti_{0.5}V_{0.5})_2AlC$, V_2AlC, Ti_3AlC_2, and Ti_3GeC_2. *Journal of Raman Spectroscopy* **2012**, *43* (1), 168–172. https://doi.org/10.1002/jrs.3036.

(19) Melchior, S. A.; Raju, K.; Ike, I. S.; Erasmus, R. M.; Kabongo, G.; Sigalas, I.; Iyuke, S. E.; Ozoemena, K. I. High-Voltage Symmetric Supercapacitor Based on 2D

Titanium Carbide (MXene, Ti_2CT_x)/Carbon Nanosphere Composites in a Neutral Aqueous Electrolyte. *J Electrochem Soc* **2018**, *165* (3), A501–A511. https://doi.org/10.1149/2.0401803jes.

(20) Mathew, K.; Sundararaman, R.; Letchworth-Weaver, K.; Arias, T. A.; Hennig, R. G. Implicit Solvation Model for Density-Functional Study of Nanocrystal Surfaces and Reaction Pathways. *J Chem Phys* **2014**, *140* (8). https://doi.org/10.1063/1.4865107.

(21) Gauthier, J. A.; Dickens, C. F.; Chen, L. D.; Doyle, A. D.; Nørskov, J. K. Solvation Effects for Oxygen Evolution Reaction Catalysis on IrO_2 (110). *The Journal of Physical Chemistry C* **2017**, *121* (21), 11455–11463. https://doi.org/10.1021/acs.jpcc.7b02383.

(22) Gray, C. M.; Saravanan, K.; Wang, G.; Keith, J. A. Quantifying Solvation Energies at Solid/Liquid Interfaces Using Continuum Solvation Methods. *Mol Simul* **2017**, *43* (5–6), 420–427. https://doi.org/10.1080/08927022.2016.1273525.

(23) Mathew, K.; Kolluru, V. S. C.; Mula, S.; Steinmann, S. N.; Hennig, R. G. Implicit Self-Consistent Electrolyte Model in Plane-Wave Density-Functional Theory. *J Chem Phys* **2019**, *151* (23). https://doi.org/10.1063/1.5132354.

(24) Björk, J.; Rosen, J. Functionalizing MXenes by Tailoring Surface Terminations in Different Chemical Environments. *Chemistry of Materials* **2021**, *33* (23), 9108–9118. https://doi.org/10.1021/acs.chemmater.1c01264.

(25) Gao, L.; Bao, W.; Kuklin, A. V.; Mei, S.; Zhang, H.; Ågren, H. Hetero-MXenes: Theory, Synthesis, and Emerging Applications. *Advanced Materials* **2021**, *33* (10). https://doi.org/10.1002/adma.202004129.

(26) Gou, J.; Zhao, L.; Li, Y.; Zhang, J. Nitrogen-Doped Ti_2C MXene Quantum Dots as Antioxidants. *ACS Appl Nano Mater* **2021**, *4* (11), 12308–12315. https://doi.org/10.1021/acsanm.1c02783.

(27) Nørskov, J. K.; Bligaard, T.; Rossmeisl, J.; Christensen, C. H. Towards the Computational Design of Solid Catalysts. *Nat Chem* **2009**, *1* (1), 37–46. https://doi.org/10.1038/nchem.121.

(28) Wang, Y.; Huang, X.; Fu, H.; Shang, J. Theoretically Revealing the Activity Origin of the Hydrogen Evolution Reaction on Carbon-Based Single-Atom Catalysts and Finding Ideal Catalysts for Water Splitting. *J Mater Chem A Mater* **2022**, *10* (45), 24362–24372. https://doi.org/10.1039/D2TA07167C.

(29) Huang, J.-J.; Liu, X.-Q.; Meng, F.-F.; He, L.-Q.; Wang, J.-X.; Wu, J.-C.; Lu, X.-H.; Tong, Y.-X.; Fang, P.-P. A Facile Method to Produce MoSe2/MXene Hybrid

Nanoflowers with Enhanced Electrocatalytic Activity for Hydrogen Evolution. *Journal of Electroanalytical Chemistry* **2020**, *856*, 113727. https://doi.org/10.1016/j.jelechem.2019.113727.

(30) Ma, T. Y.; Cao, J. L.; Jaroniec, M.; Qiao, S. Z. Interacting Carbon Nitride and Titanium Carbide Nanosheets for High-Performance Oxygen Evolution. *Angewandte Chemie International Edition* **2016**, *55* (3), 1138–1142. https://doi.org/10.1002/anie.201509758.

(31) Li, S.; Tuo, P.; Xie, J.; Zhang, X.; Xu, J.; Bao, J.; Pan, B.; Xie, Y. Ultrathin MXene Nanosheets with Rich Fluorine Termination Groups Realizing Efficient Electrocatalytic Hydrogen Evolution. *Nano Energy* **2018**, *47*, 512–518. https://doi.org/10.1016/j.nanoen.2018.03.022.

(32) Seh, Z. W.; Fredrickson, K. D.; Anasori, B.; Kibsgaard, J.; Strickler, A. L.; Lukatskaya, M. R.; Gogotsi, Y.; Jaramillo, T. F.; Vojvodic, A. Two-Dimensional Molybdenum Carbide (MXene) as an Efficient Electrocatalyst for Hydrogen Evolution. *ACS Energy Lett* **2016**, *1* (3), 589–594. https://doi.org/10.1021/acsenergylett.6b00247.

(33) Yuan, W.; Cheng, L.; An, Y.; Wu, H.; Yao, N.; Fan, X.; Guo, X. MXene Nanofibers as Highly Active Catalysts for Hydrogen Evolution Reaction. *ACS Sustain Chem Eng* **2018**, *6* (7), 8976–8982. https://doi.org/10.1021/acssuschemeng.8b01348.

(34) Liu, J.; Liu, Y.; Xu, D.; Zhu, Y.; Peng, W.; Li, Y.; Zhang, F.; Fan, X. Hierarchical "Nanoroll" like MoS2/Ti3C2Tx Hybrid with High Electrocatalytic Hydrogen Evolution Activity. *Appl Catal B* **2019**, *241*, 89–94. https://doi.org/10.1016/j.apcatb.2018.08.083.

(35) Kuang, P.; He, M.; Zhu, B.; Yu, J.; Fan, K.; Jaroniec, M. 0D/2D NiS2/V-MXene Composite for Electrocatalytic H2 Evolution. *J Catal* **2019**, *375*, 8–20. https://doi.org/10.1016/j.jcat.2019.05.019.